Monthly Notices of the ROYAL ASTRONOMICAL SOCIETY

MNRAS **542,** 747–761 (2025) https://doi.org/10.1093/mnras/staf1247
Advance Access publication 2025 July 29

Chemical abundances and Doppler imaging of the Ap Si/He-wk star HD 100357

Athul Dileep [1,2★] Santosh Joshi [1] Sofya Alexeeva,[3] Oleg Kochukhov [4] Eugene Semenko [5] Peter De Cat [6] Sebastián Zúñiga-Fernández [7] Otto Trust [8,9] Karen Pollard,[10] Lisa Crause,[11] Khalid Barkaoui [7,12,13] Michaël Gillon [7] Emmanuel Jehin[14] and Neeraj Rathore[15]

[1]*Astronomy & Astrophysics Department, Aryabhatta Research Institute of Observational Sciences, Manora Peak, Nainital 263002, Uttarakhand, India*
[2]*Department of Applied Physics, M.J.P. Rohilkhand University, Bareilly 243006, Uttar Pradesh, India*
[3]*Optical Astronomy Research Department, National Astronomical Observatories, Chinese Academy of Sciences, A20 Datun Road, Chaoyang, Beijing 100101, China*
[4]*Department of Physics and Astronomy, Uppsala University, Box 516, SE-751 20 Uppsala, Sweden*
[5]*Stellar Astrophysics Department, National Astronomical Research Institute of Thailand (NARIT), 260, Moo 4, Don Kaew, Mae Rim 50180, Chiang Mai, Thailand*
[6]*Department of Astronomy and Astrophysics, Royal Observatory of Belgium (ROB), Av. Circulaire 3, B-1180 Uccle, Belgium*
[7]*Astrobiology Research Unit, Université de Liège, Allée du 6 Août 19C, B-4000 Liège, Belgium*
[8]*Physics Department, Mbarara University of Science and Technology, P.O. Box 1410, Mbarara, Uganda*
[9]*Faculty of Science, Department of Physics, Kyambogo University, P.O. Box 1, Kyambogo, Uganda*
[10]*School of Physical & Chemical Sciences, University of Canterbury, Christchurch 8041, New Zealand*
[11]*South African Astronomical Observatory, Cape Town 7925, South Africa*
[12]*Instituto de Astrofísica de Canarias (IAC), Calle Vía Láctea s/n, E-38200 La Laguna, Tenerife, Spain*
[13]*Department of Earth, Atmospheric and Planetary Science, Massachusetts Institute of Technology, 77 Massachusetts Avenue, Cambridge, MA 02139, USA*
[14]*Space Sciences, Technologies and Astrophysics Research (STAR) Institute, Université de Liège, Allée du 6 Août 19C, B-4000 Liège, Belgium*
[15]*Department of Applied Physics, Bareilly College, Bareilly 243005, Uttar Pradesh, India*

Accepted 2025 July 25. Received 2025 July 25; in original form 2025 July 3

ABSTRACT

We present the results of time-resolved photometry, abundance analysis, and Doppler imaging of an Ap star, HD 100357. The *TESS* photometry revealed rotational modulation with a period of 1.6279247 d. Upon inspecting the residuals after removing the rotational period and its harmonics, we found additional frequencies around 15.8054 d^{-1}, which we later confirmed with ground-based observations as originating from a nearby star. Using high-resolution spectroscopy, we identified HD 100357 as an Ap Si/He-wk star exhibiting rotational modulation caused by surface abundance spots. The stellar parameters of HD 100357 were determined as $T_{\rm eff} = 11\,850$ K, $\log g = 4.57$, $\upsilon \sin i = 60$ km s^{-1}, and an inclination angle $i = 72^{\circ}$. The detailed abundance analysis revealed strongly overabundant stratified silicon, an overabundance of iron-peak elements and rare earth elements combined with remarkably deficient helium. Mapping of Fe and Cr abundances revealed the existence of ring-shaped regions with a lower concentration of the elements. Their geometry might reflect the orientation of the hypothetical magnetic field of the star, oriented $\sim 90^{\circ}$ to the rotational axis. HD 100357, with its strong chemical peculiarities and indications of possible magnetic fields, represents an interesting candidate for follow-up spectropolarimetric observations aimed at investigating its magnetic field topology and stellar activity.

Key words: line: profiles – stars: abundances – stars: chemically peculiar – stars: individual: HD100357 – stars: rotation – stars: starspots.

1 INTRODUCTION

Approximately 10 per cent of main-sequence B- and A-type stars exhibit strong globally organized magnetic fields (up to ∼30 kG) and unusually slow rotation ($\upsilon \sin i < 100$ km s^{-1}) (Sikora et al. 2019), while some exceptions have faster rotations (Mikulášek et al. 2022). These stars, known as magnetic chemically peculiar (CP) stars, display surface abundance anomalies that correlate with effective temperature. The cooler CP stars, classified as Ap SrCrEu stars (7000 K $\leq T_{\rm eff} \leq$ 10 000 K), show pronounced overabundances of Sr, Cr, and rare earth elements (REEs), whereas the hotter Ap Si and He-weak stars (10 000 $\leq T_{\rm eff} \leq$ 15 000 K) exhibit significant Si enhancements and He deficiencies (Landstreet et al. 2007; Romanyuk et al. 2013).

Preston (1974) divided CP stars into four main categories: Am (CP1), Ap (CP2), HgMn (CP3), and He-weak (CP4). Of these, CP2 and CP4 stars possess strong global magnetic fields, with strengths

★ E-mail: dileep@aries.res.in

typically ranging from a few hundred gauss to several tens of kilogauss (Aurière et al. 2007; Elkin et al. 2010; Shultz et al. 2019). In contrast, CP1 and CP3 stars are of non-magnetic nature. He-weak stars, in particular, are typically early B-type stars that exhibit strong underabundances of helium and overabundances of elements such as Si, P, and Ga (Norris 1971; Zboril & North 1997). The He deficiency in these stars is believed to arise from helium gravitational settling and inhibited mixing in the presence of magnetic fields (Vauclair & Vauclair 1975).

The anomalies in CP stars are explained by atomic diffusion, in which radiative levitation of certain heavy ions and gravitational settling of lighter ions occur in the absence of convective mixing (Michaud 1970; Richard, Michaud & Richer 2001; Alecian 2018a, b). The quenching of mixing in magnetic stars is thought to result from magnetic braking that slows stellar rotation during early evolutionary stages (Fleck 1980), promoting atmospheric stability.

The magnetic fields in CP stars not only govern diffusion but also suppress differential rotation and convective turbulence, producing horizontal abundance patches across the stellar surface. These spots rotate with the star, giving rise to photometric and spectroscopic variability on rotational time-scales. Such variability can be used to infer stellar rotation periods and map surface inhomogeneities via Doppler Imaging (DI) and Zeeman Doppler Imaging (Kochukhov et al. 2004; Donati et al. 2006). Rotation periods of magnetic CP stars span a wide range, from less than a day to several decades, with very long periods associated with the most strongly magnetic examples (Mathys 2017; Giarrusso et al. 2022; Mathys et al. 2024).

In addition to surface inhomogeneities, vertical stratification in the stellar atmosphere causes different chemical elements to concentrate at different depths. This enables the use of lines forming at different atmospheric layers to probe depth-dependent pulsation modes, particularly in a cooler subset of the magnetic CP stars that pulsate in high-overtones low-degree non-radial p-modes aligned with their magnetic axes, known as the rapidly oscillating Ap (roAp) stars (Baldry, Kurtz & Bedding 1998; Kochukhov & Ryabchikova 2001; Mkrtichian, Hatzes & Kanaan 2003; Ryabchikova et al. 2004). The strong chemical peculiarities and magnetic field in the presence of pulsations provide great insights into stellar interiors (Joshi & Joshi 2015; Kurtz 2022) and are among the best laboratories for studying magneto–acoustic interactions in stellar atmospheres (Kurtz 2000; Saio 2005).

The Nainital–Cape (N-C) Survey is one of the most extensive ground-based campaigns aimed at detecting and characterizing rapidly oscillating Ap (roAp) stars in the Northern and Southern hemispheres. Using the 1.04-m Sampurnanand Telescope at ARIES, Nainital, and the 0.5-m telescope at the South African Astronomical Observatory (SAAO), hundreds of targets were monitored over nearly two decades. The key results of this systematic survey are summarized in Ashoka et al. (2000), Martinez et al. (2001), Joshi et al. (2003, 2006, 2009, 2010, 2012, 2016, 2017, 2022), and have contributed significantly to the discovery of new roAp candidates and the understanding of the low-amplitude variability in CP stars. We continue this study by investigating the photometric variability in CP star candidates from the N-C survey using space-based missions.

In this paper, we present a comprehensive investigation of the southern Ap Si/He-wk star HD 100357 (reported a null result for pulsation in the N-C survey) using both ground-based photometric and spectroscopic observations, as well as space-based data from the *TESS* mission. This work expands the sample of Ap Si/He-wk stars in the southern sky, which serve as a transitional class between CP2 and CP4 stars, providing insights into the interactions among magnetism, rotation, and chemical stratification in CP stars.

The manuscript is structured as follows. Section 2 discusses the observations and data preparation. In Section 3, we determine the stellar parameters for the star. The chemical compositions and determination of the surface distribution of Fe and Cr are outlined in Section 4 and Section 5, respectively. Finally, the summary and conclusion drawn from our findings are given in Section 6.

Table 1. Observational log of *TESS* data. The cadence and duration of observations are given in seconds and days, respectively.

TESS Sector	Observation period	Cadence (s)	Duration (d)
10	2019 March 26–April 21	120	25.27
11	2019 April 22–May 20	1800	26.04
37	2021 April 2–April 28	600	24.15
38	2021 April 29–May 26	600	25.74
64	2023 April 6–May 4	120	26.29
65	2023 May 4–June 1	120	27.25

2 OBSERVATIONS AND DATA ANALYSIS

2.1 Photometry

2.1.1 TESS

TESS is an all-sky survey telescope whose primary objective is to detect exoplanets orbiting nearby bright stars using the transit method (Ricker et al. 2015). In addition to the primary mission, *TESS* also provides high-precision time-series photometry suitable for studying other types of variability, such as rotational, pulsational, or eclipses of stars brighter than 12th magnitude (Sullivan et al. 2015; Bowman et al. 2022). *TESS* target pixel files (TPFs) and light-curve files are available in short cadences of 20 and 120 s, while full-frame images are obtained in long cadences: 1800 s for Sectors 1–26 (Cycles 1–2), 600 s for Sectors 27–55 (Cycles 3–4), and 200 s from Sector 56 onwards (Cycle 5+). These data products are publicly available and can be downloaded through the Mikulski Archive for Space Telescopes (MAST).[1]

HD 100357 was observed in six different sectors by *TESS* and the log of observations is given in Table 1. The *TESS* light-curve files contain two types of flux, namely, the Simple Aperture Photometry (SAP) flux and the Pre-search Data Conditioning SAP (PDCSAP) flux. In the PDCSAP flux, long-term instrumental trends are removed using co-trending basis vectors (Smith et al. 2012). For this study, we used 120, 600, and 1800 s cadence PDCSAP flux downloaded from the MAST archive via the LIGHTKURVE Python package (Lightkurve Collaboration 2018).

The light-curve fluxes were converted to relative magnitudes (mmag) and centred at zero by subtracting the mean magnitude. Light curves were then stitched together and subjected to frequency analysis to identify the rotational frequency using the discrete fourier fitting technique implemented in the PERIOD04 package (Lenz & Breger 2005, 2014). We fitted the fundamental rotational frequency and its 15 consecutive integer multiples (harmonics) simultaneously using a multicomponent sinusoidal model and performed subsequent pre-whitening to identify any higher frequencies. A signal-to-noise

[1] https://archive.stsci.edu/

Table 2. Frequency, amplitude, and S/N from the combined light curves of all six sectors. f_{rot} is the rotational frequency, and the harmonics are given as integer multiples of this frequency. The labels 'f_{n*}', $n = 1$, 2, and 3 indicate the frequencies of the contaminating star.

	Frequency (d^{-1})	Amplitude (mmag)	S/N
$2f_{rot}$	1.2285581(3)	17.733(6)	545.2
f_{rot}	0.6142790(1)	8.520(6)	140.8
$4f_{rot}$	2.457116(3)	0.762(6)	54.8
$3f_{rot}$	1.842837(8)	0.281(6)	15.0
$5f_{rot}$	3.07140(2)	0.122(6)	10.1
$7f_{rot}$	4.29995(2)	0.099(6)	11.7
$10f_{rot}$	6.14279(3)	0.085(6)	11.7
$12f_{rot}$	7.37135(4)	0.060(6)	9.1
$8f_{rot}$	4.91423(4)	0.059(6)	7.3
$14f_{rot}$	8.59991(4)	0.052(6)	8.9
f_{1*}	15.80501(3)	0.087(6)	15.6
f_{2*}	14.32267(6)	0.038(6)	6.5
f_{3*}	16.98574(7)	0.034(6)	5.7

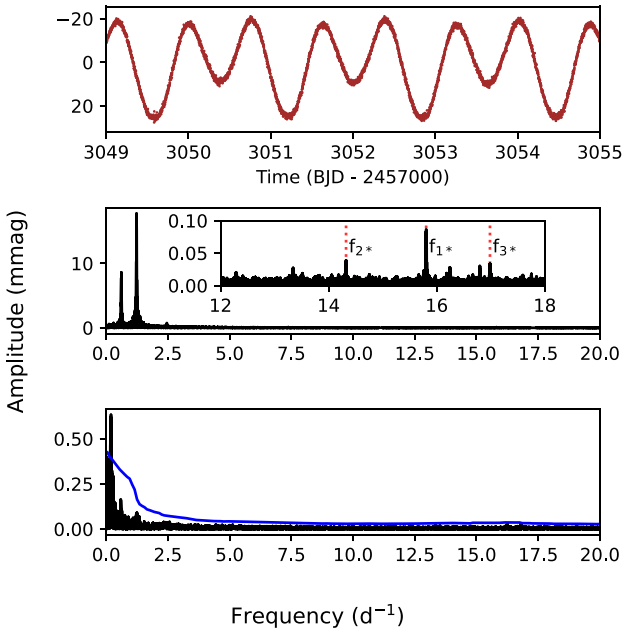

Figure 1. The top panel displays a segment of the *TESS* light curve with a cadence of 120 s. The second panel shows the amplitude spectrum using the combined light curve from all *TESS* sectors. The inset in the second panel shows the frequency range from 12 to 18 d^{-1}, where contaminating signals in the residuals persist after fitting and eliminating 15 successive harmonics of the fundamental rotational frequency. The third panel shows the residual after removing all the significant frequencies, where the blue line represents the 5.3 S/N level. The low-frequency peaks in the residuals can be instrumental artefacts.

ratio (S/N) greater than 5.3 was adopted as the criterion for selecting significant frequencies, based on the detection threshold for *TESS* sectors by Baran & Koen (2021). The derived frequencies, amplitudes, and S/N values obtained are listed in Table 2. The light curve, frequency spectrum, and residuals are shown in Fig. 1.

HD 100357 (TIC 280667311) was classified as an Ap star with A0 spectral type and showing EuCrSr type peculiarity by Houk & Cowley (1975). These stars are known to show rotational variability due to chemical abundance spots. Bernhard, Hümmerich & Paunzen (2020) reported a rotational period of 1.62794 d for HD 100357 star using ground-based ASAS-3 data. In our frequency analysis, we detected a rotational period in agreement with the previous value and nine additional harmonics. Interestingly, the amplitude of the first harmonic is higher than the fundamental rotational frequency, indicating the presence of multiple features located on diametrically opposite sides of the star's visible surface. We performed a parabolic fit to the peak of each light maximum identified in all *TESS* sectors to obtain the accurate timings and finally fitted the linear ephemeris for this star. The updated linear ephemeris is

$$\mathrm{BJD_{max}} = 2458570.9785(3) + 1.6279247(7) \times E, \quad (1)$$

where $\mathrm{BJD_{max}}$ is the time of light maxima at epoch E.

2.1.2 *TRAPPIST-South*

We conducted ground-based follow-up observations in the field surrounding HD 100357 using the TRAPPIST-South telescope. It is a 60-cm Ritchey–Chretien telescope located at ESO-La Silla Observatory in Chile. It is equipped with a thermoelectrically cooled 2K×2K FLI Proline CCD camera with a field of view of 22 arcmin × 22 arcmin and a pixel scale of 0.65 arcsec pixel^{-1} (Gillon et al. 2011; Jehin et al. 2011). The observations were carried out on 2025 March 18 over a duration of 4 h, with individual exposures of 10 s, through the standard Johnson–Cousins *R*-band filter. We used the python package `Prose`[2] (Garcia et al. 2022) for analysing the images and subsequently performing differential photometry. The primary aim of these observations was to assess the possible contamination in the *TESS* light curve of HD 100357.

2.1.3 *Contamination*

After fitting and subtracting the rotational frequency and its harmonics from the time-series data, the residuals show low-amplitude frequencies at 15.805, 14.323, and 16.986 d^{-1} (see inset of middle panel of Fig. 1). Since the *TESS* pixels have poor spatial resolution (21 arcsec), the contamination of signals from nearby bright stars is expected. To mitigate this, we performed a pixel-by-pixel investigation of the *TESS* TPF to check for any contamination. We used the technique described in Dileep et al. (2025), by selecting custom apertures around the target star identified through *Gaia* DR3 positions (Gaia Collaboration 2023) (See Fig. B1). Our finding is that the additional frequencies detected in the residuals of HD 100357 (Gmag = 8.98) originated from a nearby star (*Gaia* DR3 5236626819707864192; Gmag = 13.01; ΔGmag = 4.03), possibly a new δ Scuti star. We further confirmed the origin of these frequencies with ground-based observations from the TRAPPIST-South telescope, which has a spatial resolution 30 times better than that of *TESS*, allowing the contaminating star to be fully resolved in the corresponding CCD frames. Fig. B2 shows the folded light curve using the dominant contaminating frequency of 15.8054 d^{-1}, along with a CCD image of the field that marks the stars. Apart from this, there is a very close visual companion to the star that can cause contamination, which will be discussed in the following section.

2.2 *Gaia* astrometry

HD 100357 was classified as a visual double star in the Washington Double Star Catalogue (Mason et al. 2001) and the Tycho Double Star Catalogue (Fabricius et al. 2002). *Gaia* DR2 (Gaia Collaboration

[2]https://prose.readthedocs.io/en/latest/ipynb/sources.html

Table 3. Log of spectroscopic observations of HD 100357 in the chronological orders. The rotational phase, RV, and projected rotational velocity ($\upsilon \sin i$) are also listed. The rotational phases were calculated with reference time, $t_0 = 2458570.9785$ BJD.

Telescope	Diameter (m)	Spectrograph	Phase	Date	BJD (2400000+)	Resolution	Integration (s)	S/N (@550nm)	RV (km s^{-1})	vsini ($\pm$ 2 km s^{-1})
MPG/ESO	2.2	FEROS	0.938	2007 Feb 8	54139.6498	48 000	800	133	-4.2 ± 0.3	56
SALT	10.0	HRS	0.334	2023 Jan 14	59958.5137	37 000	300	74	-3.1 ± 0.4	63
McLellan	1.0	HERCULES	0.614	2023 Dec 25	60304.0915	41 000	1800	45	2.7 ± 0.5	56
			0.628	2023 Dec 25	60304.1135	41 000	1800	51	-1.5 ± 0.5	60
			0.839	2023 Dec 27	60306.0830	41 000	1800	18	-2.0 ± 1.0	63
			0.235	2023 Dec 31	60309.9862	41 000	1800	41	-1.6 ± 0.6	62
			0.249	2023 Dec 31	60310.0082	41 000	1800	34	-1.2 ± 0.5	61
			0.264	2023 Dec 31	60310.0324	41 000	1800	33	-2.1 ± 0.5	63
			0.277	2023 Dec 31	60310.0544	41 000	1800	45	-1.7 ± 0.4	63
			0.883	2024 Jan 1	60311.0397	41 000	1800	53	-1.6 ± 0.4	61
			0.896	2024 Jan 1	60311.0617	41 000	1800	53	-1.1 ± 0.4	61
			0.513	2024 Jan 2	60312.0662	41 000	1800	59	-1.6 ± 0.4	60
			0.528	2024 Jan 2	60312.0896	41 000	1800	44	-0.9 ± 0.4	60
			0.461	2024 Jan 23	60333.1452	41 000	1800	40	-4.0 ± 0.5	59
			0.925	2024 Feb 19	60359.9473	41 000	1800	30	-3.0 ± 0.6	58
			0.939	2024 Feb 19	60359.9693	41 000	1800	39	-3.3 ± 0.5	57
			0.561	2024 Feb 20	60360.9817	41 000	1800	67	0.1 ± 0.4	60
			0.574	2024 Feb 20	60361.0037	41 000	1800	63	0.9 ± 0.4	58
			0.184	2024 Feb 21	60361.9966	41 000	1800	65	-1.6 ± 0.4	61
			0.198	2024 Feb 21	60362.0186	41 000	1800	55	-1.5 ± 0.4	61

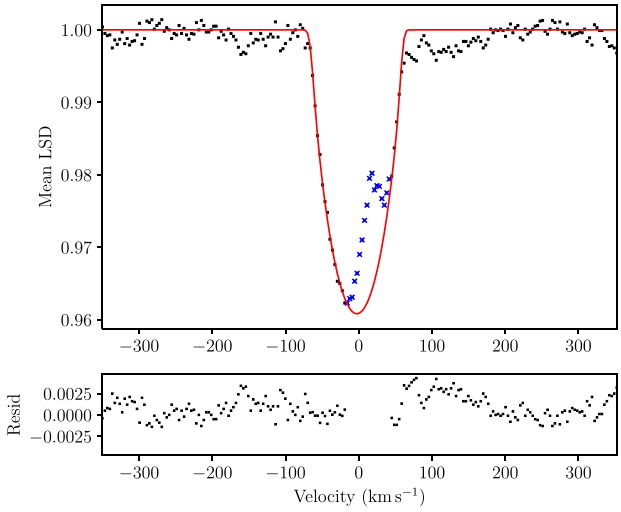

Figure 2. Top panel: the scattered points represent the LSD profile of HD 100357 obtained from SALT spectrum. The solid curve is the best-fitting rotationally broadened line profile. The points in the middle, represented by cross symbols, are excluded from the line profile fit. Bottom panel: the residuals of the best-fitting line profile to the observed LSD profile.

2018) and DR3 (Gaia Collaboration 2023) catalogues also reported this companion star. From the *Gaia* DR3 position and parallax, they are separated by ∼2.55 arcsec in the sky and ∼5.33 pc apart in space. Brandt (2021) and Kervella, Arenou & Thévenin (2022) searched for proper motion anomalies in several stars using the Hipparcos and *Gaia* proper motions and parallax, but they did not report any significant proper motion anomaly for HD 100357. Hence, we can conclude that these are comoving stars with no orbital interaction. Nevertheless, the nearby visual companion with a *Gaia* G magnitude of 12.35 compared to the target's $G = 8.98$ may cause flux contamination in the *TESS* pixels at a level of approximately 5.7 per cent. Since we did not detect any additional variability from this nearby companion, it will only add a constant noise level to the signal from HD 100357; hence, one can neglect the contamination in this case.

2.3 Spectroscopy

We acquired 20 high-resolution spectra for the spectroscopic analysis of HD 100357. One spectrum was taken with the High Resolution Échelle Spectrograph (HRS) (Tyas 2012) attached to the 10.0-m Southern African Large Telescope (SALT) of the South African Astronomical Observatory (Sutherland, South Africa) with spectral resolution $R \approx 37\,000$ over the wavelength range 370–890 nm. We retrieved one archival spectrum with a spectral resolution R≈48 000 over 350–920 nm, from the Science Portal of the European Southern Observatory (ESO)[3] that was observed with the Fiberfed Extended Range Optical Spectrograph (FEROS) (Kaufer et al. 1999) at MPG/ESO 2.2-m telescope (La Silla, Chile) under the programme ID 078.D-0080(A). Finally, a dedicated program was carried out with the High Efficiency and Resolution Canterbury University Large Échelle Spectrograph (HERCULES) (Hearnshaw et al. 2002), equipped on the 1-m McLellan telescope of Mount John University Observatory (Mount John, New Zealand). In total, 18 HERCULES spectra were collected with a spectral resolution of R≈41 000 over the wavelength range 380–880 nm. The standard reduction, wavelength calibration, and continuum normalization of HERCULES spectra were performed using the dedicated pipeline HRSP (Skuljan 2004), while the HRS spectrum was reduced and wavelength calibrated using the SALT HRS pipeline (Crawford et al. 2010; Kniazev, Gvaramadze & Berdnikov 2016, 2017). The HRS and FEROS spectra were then continuum normalized using the CONTINUUM task of the IMAGE REDUCTION AND ANALYSIS FACILITY[4] (IRAF). For the in-depth spectroscopic analysis, all these spectra were corrected for the barycentric motion. We calculated the S/N for each spectrum at a wavelength of 5500 Å. The log of spectroscopic observations is given in Table 3.

2.3.1 *Least-squares deconvolution*

Magnetic CP stars show significant line profile variations as a result of chemical spots on their surface. These variations are difficult to detect when the S/N of a spectrum is very low. To overcome this difficulty, the least-squares deconvolution (LSD) technique (Donati & Brown 1997; Kochukhov, Makaganiuk & Piskunov 2010) is used to get a higher S/N mean line profile using a large number of metallic lines. We constructed the LSD profiles for the observed spectra of HD 100357 using a line mask prepared with the atomic data extracted from the VALD3 data base (Piskunov et al. 1995; Ryabchikova et al. 2015; Pakhomov, Ryabchikova & Piskunov 2019). We avoided the broad Balmer lines and the interstellar Na lines for constructing the LSD profiles. We fitted a rotationally broadened profile to the LSD profiles, excluding the core areas (see Fig. 2), where line profile variations occur, to derive the radial velocities (RVs) and $\upsilon \sin i$ values for each observation. The results derived from the LSD profiles are shown in the last two columns of Table 3.

3 STELLAR PARAMETERS

3.1 Photometric parameters

To estimate the effective temperature, $T_{\rm eff}$, and surface gravity, $\log g$, of our target, we used photometric data published in the General Catalogue of Photometric Data[5] (Mermilliod, Mermilliod & Hauck 1997) for the Strömgren and Geneva systems. HD 100357 is located close to the Galactic equator, a region having significant interstellar reddening. A colour excess of $E(B-V) = 0.10$ mag was determined from the intensity of the Na D1 line, following the calibration by Munari & Zwitter (1997), and the parallax is $\pi = 2.72 \pm 0.02$ mas (Gaia Collaboration 2021). In addition, we used the 3D dust map G-Tomo[6] (Lallement et al. 2022; Vergely, Lallement & Cox 2022) to derive the colour excess $E(B-V) = 0.136$, which is in good agreement with the value derived from the Na D1 line.

Using the calibrations given by Napiwotzki, Schoenberner & Wenske (1993) for indices in Strömgren system results in the estimated $T_{uvby} = 12,420$ K and $\log g = 4.56$. At the same time, the effective temperature calibrated using index $[u-b]$ turns out to be 1000 K lower: 11 050 K. It is a typical feature of CP stars with strong chemical anomalies. In light of anomalies, it sounds reasonable to apply the special relation from equation (12) of the original publication. This brings us $T_{[u-b]}(\mathrm{Ap}) = 10750$ K. Unfortunately, Napiwotzki et al. (1993) did not provide the method to estimate

[3] https://archive.eso.org/scienceportal/home

[4] https://iraf-community.github.io/

[5] https://gcpd.physics.muni.cz/

[6] https://explore-platform.eu/sdas/about/gtomo

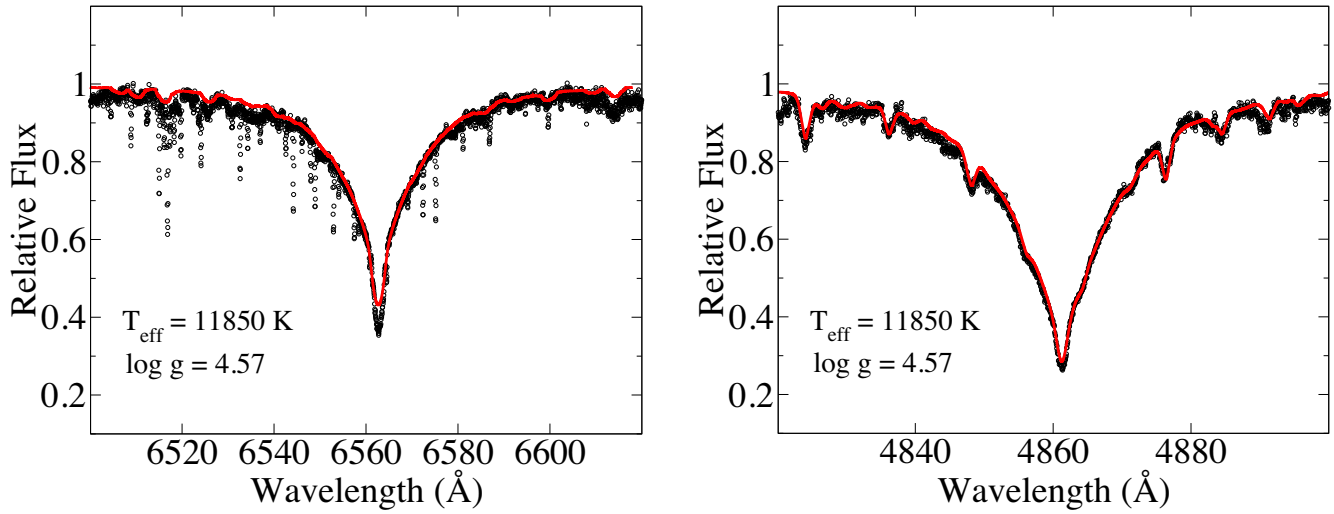

Figure 3. Comparison of the observed spectrum (black circles) and synthetic spectrum (red line) in the region of H_α(left panel) and H_β (right panel). The telluric lines near the H_α region were excluded during the fitting.

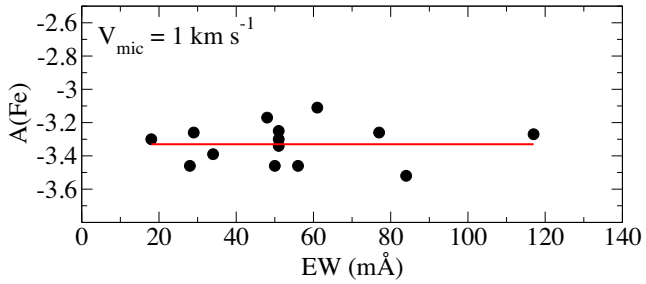

Figure 4. The scatter points represent iron abundances as a function of their equivalent widths for HD 100357. The solid straight line is the optimal minimised slope of this relationship at $\xi_{\rm mic} = 1\ km\ s^{-1}$.

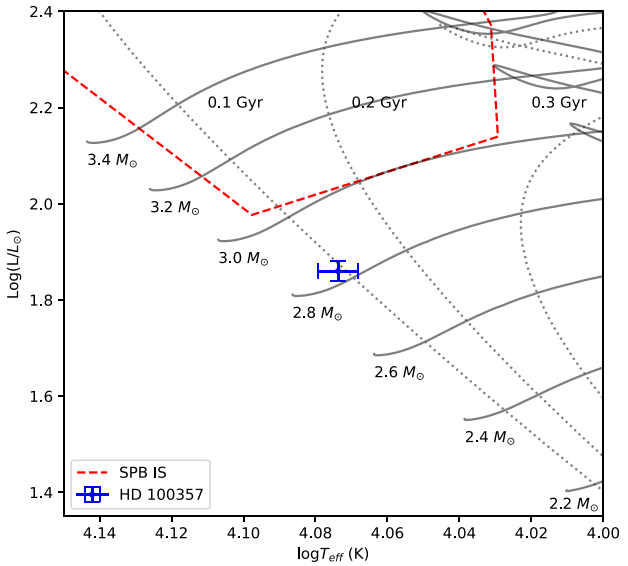

Figure 5. Position of HD 100357 in the H-R diagram with error bars. The dotted lines and the solid lines represent the isochrones and the evolutionary tracks, respectively. The dashed line is the instability strip of slowly pulsating B stars (Miglio, Montalbán & Dupret 2007).

Table 4. Summary of all stellar parameters of HD 100357 as ascertained from this study. The associated error bars for the last digits of the relevant values are shown in brackets.

Parameters	Values
$P_{\rm rot}$ (d)	1.6279294 (7)
t_0 (BJD)	2458570.9743 (4)
Vmag	8.97 (2)
E(B-V)	0.136 (2)
$\log(L/L_\odot)$	1.86 (2)
$T_{\rm eff}$ (K)	11 850 (150)
$\log g$	4.57 (5)
[Fe/H]	1.16 (12)
$\upsilon \sin i$ (km s^{-1})	60 (2)
$\xi_{\rm mic}$ (km s^{-1})	1.0 (2)
R ($R_\odot$)	2.03 (10)
i (deg)	72 (11)
M ($M_\odot$)	2.83 (4)
Age (Gyr)	0.09 (4)

the errors. Following the common practice, it would be reasonable to assume that the typical error of $T_{\rm eff}$ is close to 300 K, while for $\log g$ one can expect an error of order 0.15. To account for the interstellar reddening in the Geneva data, we converted $E(B-V)$ to $E(B2-V1)$ by dividing it by 1.14.

Calibrations published by Kunzli et al. (1997) for the Geneva system, depending on the expected metallicity, give two sets of data: $T_{\rm Geneva} = 11\,726$ K and $\log g = 4.59$ for the case of $[M/H] = 0$, or $T_{\rm Geneva} = 11\,560$ K and $\log g = 4.56$ when $[M/H] = +1$. The estimated error of determination is 75 K for $T_{\rm eff}$ and 0.07 for $\log g$.

As the problem of finding basic parameters from photometry is especially acute, we also revised the mentioned parameters found from the original calibrations in the framework of the study by Netopil et al. (2008). This gives the corrected values: $T'_{uvby} = 11\,480$ K and $T'_{\rm Geneva} = 10\,975$ K.

To summarize, we can state that photometry cannot give consistent estimations of the effective temperature. We can sort all results into two groups with the mean values: $T_{\rm orig} = 11\,900$ K and $T_{\rm Ap} = 11\,070$ K. The first value is used as the effective temperature

Table 5. The mean LTE abundances of chemical species in HD 100357. The parameter [X/H] = log (N_X/N_H) − log $(N_X/N_H)_\odot$ compares the observed abundances with solar abundances (Lodders 2021). The last column of the table lists the standard deviations for each species when more than two lines are available.

Atomic number	Ion	Number of lines	log $(A)_X$	[X/H]	Sigma
2	He II	2	−3.1	−2	–
6	C II	1	−4.7	−1.28	–
8	O I	1	−4.27	−1.03	–
12	Mg II	3	−5.03	−0.53	0.15
13	Al II	3	−5.98	−0.39	0.03
14	Si II	19	−3.7	0.78	0.31
14	Si III	1	−3.5	0.98	–
15	P II	2	−5.55	1.03	0.07
16	S II	2	−4.25	0.63	0.07
21	Sc II	3	−7.27	1.58	0.11
22	Ti II	4	−6.28	0.75	0.14
24	Cr II	11	−4.11	2.27	0.11
25	Mn I	1	−4.45	2.1	–
25	Mn II	11	−4.49	2.06	0.08
26	Fe II	14	−3.33	1.16	0.12
27	Co II	2	−5	2.04	–
28	Ni I	3	−5.8	−0.08	0.01
38	Sr II	1	−5.41	3.67	–
60	Nd III	2	−7.27	3.28	0.1
64	Gd II	2	−5.62	5.27	0.17
66	Dy II	2	−6.94	3.94	0.02

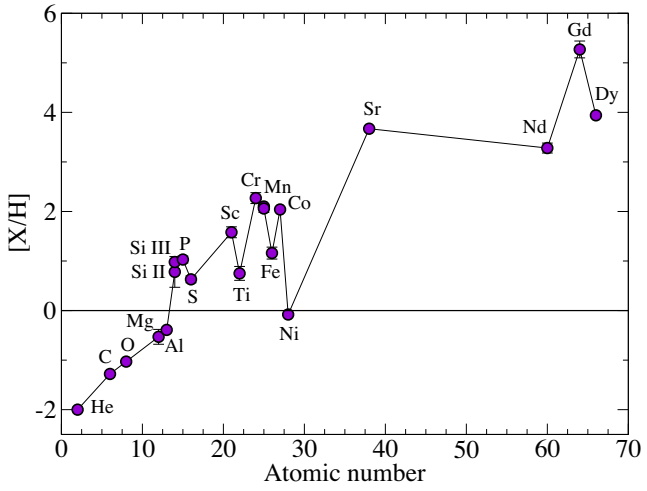

Figure 6. Relative photospheric abundance of chemical species of HD 100357 at rotational phase 0.334. The horizontal line at zero denotes the solar reference. There is an excess of Si, Fe-peak elements, and heavier elements, accompanied by a deficiency of light elements and a pronounced underabundance of He.

of HD 100357 through this study. However, we cannot exclude that the real $T_{\rm eff}$ can be lower by about 1000 K. As for the surface gravity, we adopted the mean value, $\log g = 4.57 \pm 0.15$, which still appears overestimated.

3.2 Distance, luminosity, and radius

The distance of a star can be determined by the *Gaia* DR3 parallax. The parallax angle $\pi = 2.72 \pm 0.02$ mas results in the distance of our target $d = 367 \pm 3$ pc. We calculated the extinction in the V band $A_v = R_v \times E(B-V)$, where R_v=3.1 (Cardelli, Clayton & Mathis 1989). We estimated the bolometric correction (BC = −0.65) using the empirical relation given by Torres (2010). For calculating the Johnson V magnitude of the star, we used the conversion from Tycho V_T and B_T magnitude (Bessell 2000), resulting in the apparent magnitude, $V = 8.97 \pm 0.02$. This yields the value of $\log(L/L_\odot)$=1.86 ± 0.02 $L_\odot$. The radius of the star is calculated from the Stefan–Boltzmann equation, and the value is $R = 2.03 \pm 0.10\ R_\odot$.

3.3 Inclination angle

The inclination angle of the rotation axis of a magnetic CP star is required to model the abundance spot on the surface of the star and determine the geometry of the magnetic fields (Stibbs 1950; Kochukhov 2017). The equatorial velocity of a rotating star can be calculated as $v_{eq} = 2\pi R/P$, where R is the radius of the star and P is its rotational period. We used the rotational period determined from the *TESS* data, and mean $\upsilon \sin i$ (60 ± 2 km s^{-1}) calculated from the spectroscopy, giving an inclination angle, $i = 72^\circ \pm 11^\circ$.

3.4 Spectroscopic parameters

The absorption-line spectrum of HD 100357 aligns with that of an early A-type photosphere. Comparison with the spectral standards from Gray & Corbally (2009) shows that He I lines are weak across a wide spectral range. In contrast, lines of Si II, Sc II, Ti II, Cr II, Mn II, Fe II, Co II, and Sr II are unusually strong. Notably, the Mg II 4481 Å line, which is typically one of the strongest, appears relatively shallow in the spectrum of HD 100357, which is a typical feature of He-weak stars.

The atmospheric parameters of HD 100357 were determined using a self-consistent iterative approach based on spectral synthesis, utilizing the SALT HRS spectrum. As a starting point, we adopted the effective temperature ($T_{\rm eff}$ = 11 900 K) and surface gravity ($\log g$ = 4.57) derived from photometric data. In the subsequent step, a He-weak atmospheric model with a hydrogen abundance of N_H/N_{tot} = 0.99 was computed using the ATLAS12 model atmosphere code (Castelli 2005; Kurucz 2005) that accounts for the impact of chemical composition anomalies on the atmospheric opacity distribution.

Theoretical spectra were computed assuming local thermodynamic equilibrium (LTE) using this model atmosphere and atomic data obtained from the VALD3 data base (Piskunov et al. 1995; Ryabchikova et al. 2015; Pakhomov et al. 2019) with the `synthV_NLTE` code (Tsymbal, Ryabchikova & Sitnova 2019). To compare the theoretical stellar spectra with observational data, we utilized the widget program `BinMag`[7] (Kochukhov 2018) that interfaces to the `synthV_NLTE` code and allows for automatic determination of the best fits to the observed line profiles, enabling determination of highly accurate chemical abundances.

The $T_{\rm eff}$ and $\log g$ parameters were refined by comparing the synthetic spectrum to the observed spectrum in the wings of the H_α and H_β hydrogen lines. Fig. 3 presents a comparison between the observed and synthetic profiles calculated using this final set of parameters. The microturbulent velocity, $\xi_{\rm mic} = 1$ km s^{-1}, was determined using the classical method of minimizing the slope in the relationship between elemental abundance and equivalent widths (see Fig. 4). The equivalent widths were derived using synthetic line-profiles, accounting for blending due to rotational broadening

[7] http://www.astro.uu.se/~oleg/binmag.html

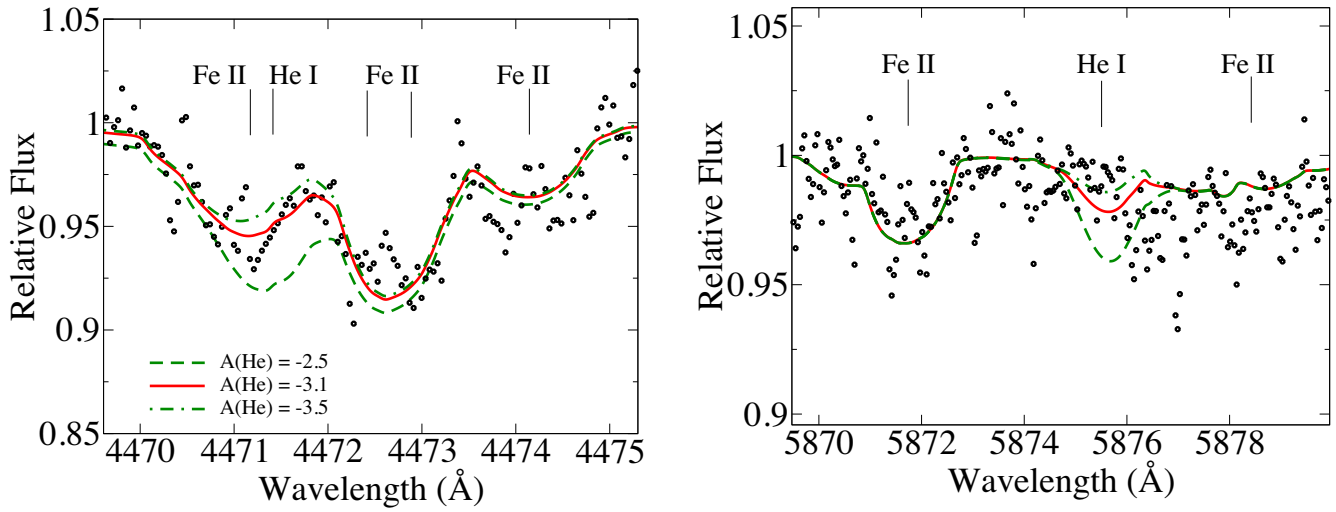

Figure 7. Observed He I λ4471 Å (left panel) and He I λ5876 Å (right panel) line profiles for HD 100357 (black circles), compared to synthetic profiles (red and green lines). The red solid lines were obtained assuming the best He abundance A(He) = −3.1. The green dashed lines show the synthetic profile by increasing He to A(He) = −2.5 value. The green dash–dotted lines show the synthetic profile by decreasing He to −3.5. The nearby blended lines of Fe II are also indicated.

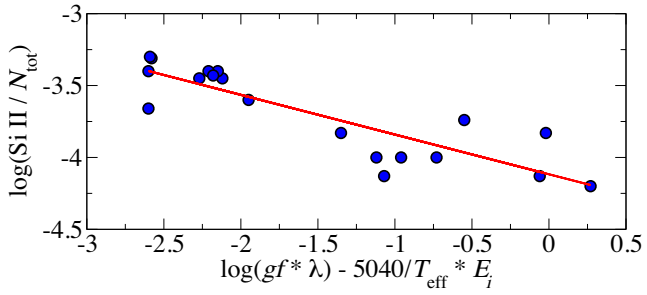

Figure 8. The scattered points indicate the individual Si abundances as a function of line strength in the atmosphere of HD 100357. The solid line represents a linear fit to the scattered data points, illustrating the declining abundance trend of Si with line strength, indicative of abundance stratification.

(60 km s^{-1}), ensuring that the contribution of each line was properly modelled.

Our analysis confirmed that the initial photometry-based parameters are consistent with the spectroscopic examination of the hydrogen lines. As a result, we determined the following parameters: effective temperature $T_{\rm eff} = 11\,850 \pm 150$ K, surface gravity $\log g = 4.57 \pm 0.05$, and a microturbulent velocity $\xi_{\rm mic} = 1.0 \pm 0.2$ km s^{-1}. The iron abundance is measured using 14 lines, and the average value is log A(Fe) = -3.33 ± 0.12, which reflects an overabundance relative to solar with [Fe/H] = 1.16 dex (Lodders 2021).

3.5 Evolutionary status

To determine the evolutionary status of the star, we constructed a Hertzsprung–Russell (H-R) diagram with theoretical isochrones and evolutionary tracks downloaded from MESA Isochrones and Stellar Tracks (MIST) (Choi et al. 2016; Dotter 2016) compiled using the MODULES FOR EXPERIMENTS IN STELLAR ASTROPHYSICS (MESA) code (Paxton et al. 2011, 2013, 2015, 2018). We placed our star in the H-R diagram using the determined values of log $T_{\rm eff}$ and $\log(L/L_\odot)$ with associated errors. The position of HD 100357 in the HR diagram (Fig. 5), along with the inspection of its high-resolution spectrum in Section 3.4, indicates that it is a main-sequence star. From the inspection of the isochrones and stellar tracks, one can conclude that HD 100357 has a mass $M \sim 2.83\ M_\odot$ and an age $t \sim 90$ Myr. The stellar parameters determined from our analysis in this section are listed in Table 4.

4 CHEMICAL COMPOSITION

We used the SALT HRS spectrum to determine the chemical abundances of HD 100357, which was obtained in the most recent epoch and with the best S/N. Elemental abundances were generally derived from multiple absorption lines within the observed spectral range. Abundances are expressed as $\log(A)_X = \log(N_X/N_H)$, where N_X denotes the number density of element X and N_H represents the number density of hydrogen. The abundances were determined under the LTE assumption by fitting synthetic line profiles to observed ones using the `BinMag` tool with the line list extracted from the VALD3 data base. Hyperfine splitting (Pakhomov et al. 2019) was also incorporated during the extraction of the line list. The mean abundances of each element X were calculated by averaging many lines. Uncertainties were determined as the standard deviation of the mean value when more than two lines were available. Relatively high rotational broadening complicates the task of selecting lines. Consequently, most elements in the HD 100357 spectrum are represented by a limited number of blended lines.

We derived the LTE abundances for 19 elements. The results of this analysis are summarized in Table 5 and illustrated in Fig. 6, which compares the derived abundances to solar abundances using the notation $[X/H] = \log(N_X/N_H) - \log(N_X/N_H)_\odot$. The solar reference abundances are taken from Lodders (2021). The detailed abundances from individual lines are listed in Table A1.

4.1 Helium

We identified weak absorption lines of He I at 4471 Å and 5876 Å and assessed the helium abundance as $\log(A)_{He} = -3.1$ dex, which is 2 dex lower than the solar value. Fig. 7 presents a comparison between the observed and synthetic He I profiles computed using three distinct sets of He abundances for comparison.

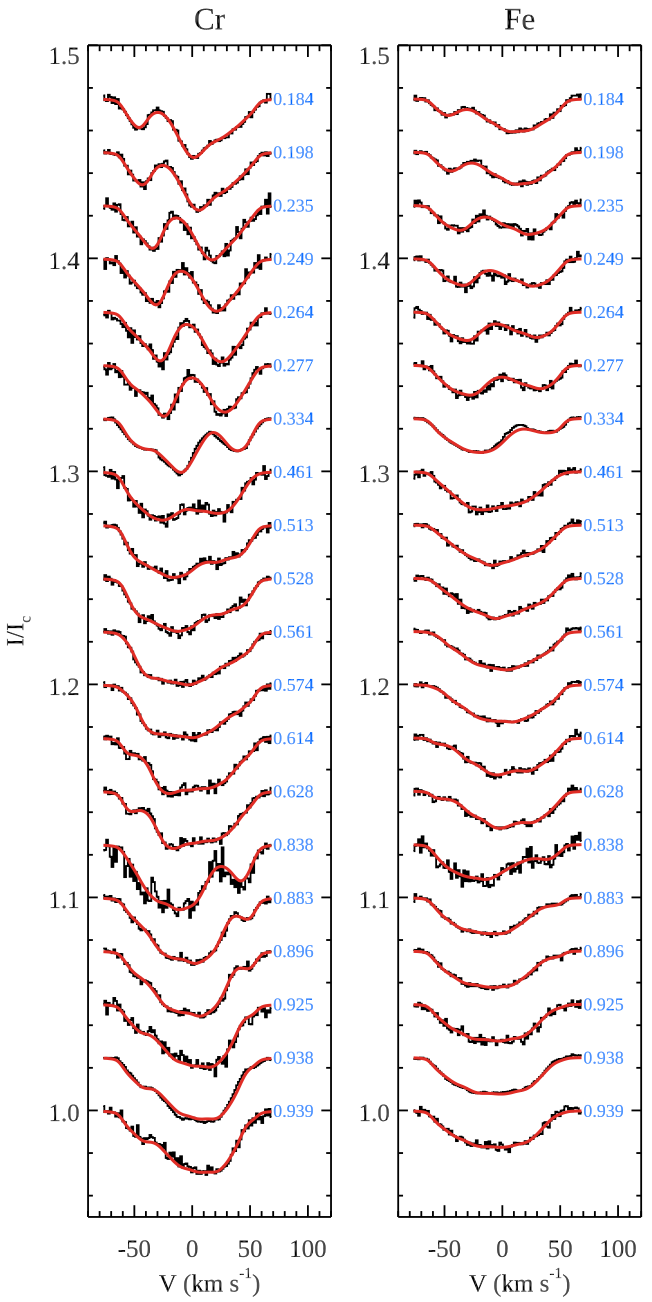

Figure 9. Comparison of the observed LSD profiles (histograms) and DI model LSD profiles (solid lines) of Cr and Fe. The profiles for different rotational phases are offset vertically. The phase values are shown to the right of the respective profiles.

4.2 Carbon, oxygen, magnesium, and aluminium

We were able to measure only one C II line at 4267.259 Å and the oxygen triplet in the wavelength range 7771–7775 Å. Carbon and oxygen are both strongly depleted by more than 1.0 dex in the atmosphere of HD 100357. Slightly less depletion was found for Mg and Al, by ∼0.4 dex compared to solar values.

4.3 Silicon

We were able to measure only one weak Si III line, which agrees well within the error bar with the mean abundance derived from Si II lines. Despite our best efforts to select primarily unblended Si II lines with varying excitation energies and oscillator strengths, we observed a significant scatter of 0.30 dex around the mean value. The big scatter in the Si II-based abundances prompted us to investigate the relationship between abundance measurements from individual lines and the line strength, which depends on oscillator strength and excitation energy (see e.g. Ryabchikova 2014). This relationship is illustrated in Fig. 8 for Si II lines. The figure shows a noticeable trend: stronger lines formed higher in the atmosphere yield lower individual abundances compared to weaker lines formed closer to the photosphere. These results suggest a clear vertical stratification of Si, where most of the Si is concentrated in the deeper layers of the star (Bailey & Landstreet 2013). A detailed analysis of vertical abundance stratification is beyond the scope of this paper.

4.4 Phosphorous, sulphur

We used two lines of P II at 4602 and 6166 Å and two lines of S II at 5454 and 5606 Å. Our estimates indicate that both P and S are overabundant, with the abundance for P being 1.03 dex higher than the solar value and a slightly lesser abundance for S by 0.63 dex.

Among the two categories of He-weak stars – magnetic and non-magnetic – non-magnetic He-weak stars occasionally show overabundances of phosphorus (up to twice the solar value) and gallium (up to five times the solar value). While phosphorus is overabundant in the atmosphere of HD 100357, no gallium lines were detected.

4.5 Iron peak elements: scandium to nickel

With the exception of nickel, which possesses an abundance close to the solar value, the remaining six iron-peak elements exhibit significant overabundances, ranging from 1.0 to 2.0 dex.

4.6 Neutron-capture elements

The abundance of Sr was measured using the Sr II λ 4215.5 Å line and shows a significant enhancement of 3.67 dex compared to the solar value. Efforts to analyse other neutron capture elements, such as Y and Zr, were unsuccessful due to a lack of suitable spectral lines for accurate abundance determination.

4.7 Rare earth elements

HD 100357 displays significant overabundances of REEs, including Nd, Gd, and Dy. Such high overabundances are a distinctive feature of upper main-sequence magnetic CP stars. A similar chemical pattern was observed in the slowly rotating strongly magnetic Ap star HD 144897, as reported by Ryabchikova et al. (2006). Owing to the high rotational velocity of HD 100357, we were able to reliably measure only three REE.

5 DOPPLER IMAGING

DI (Kochukhov 2017) is a robust technique to ascertain the topology of chemical spots on Ap stars. The technique involves mapping the surface inhomogeneities of a star given the observed line profile variations. For this, one needs high S/N (S/N∼300) line profiles of different chemical elements over adequate rotational phases. In the absence of sufficient S/N, we can use the LSD technique to produce a mean line profile with enhanced S/N appropriate for DI, where the

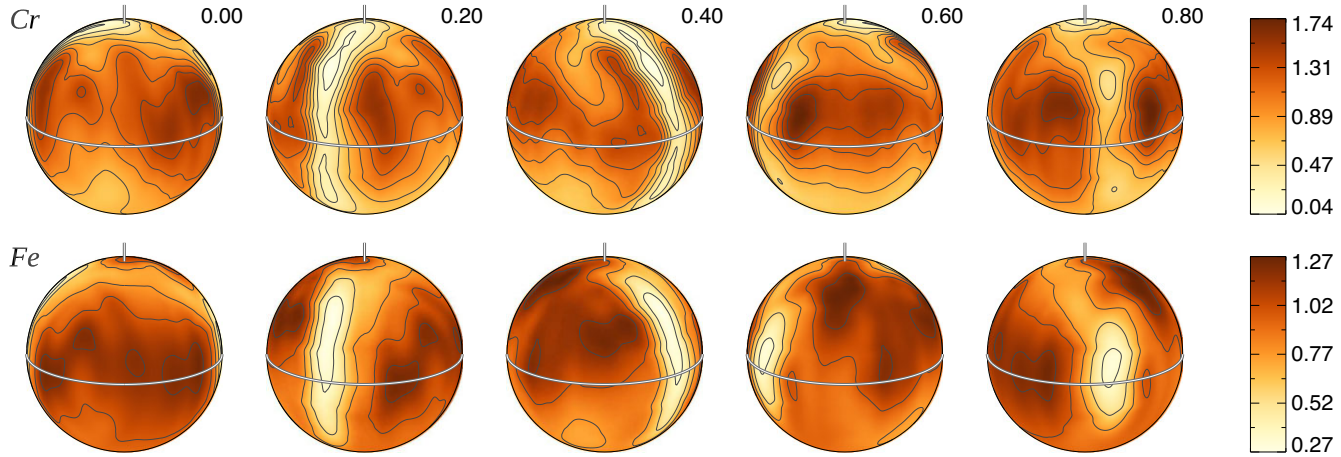

Figure 10. Surface distributions of Cr and Fe reconstructed with DI. The maps are given in terms of the logarithm of the local line strength. The star is shown at five rotational phases, indicated to the right of each column, at the inclination angle $i = 72^{\circ}$. In each spherical plot, the thick line shows the stellar equator, whereas the short bar corresponds to the rotational pole. We can notice a ring of underabundance regions inclined at 90° to the stellar equator.

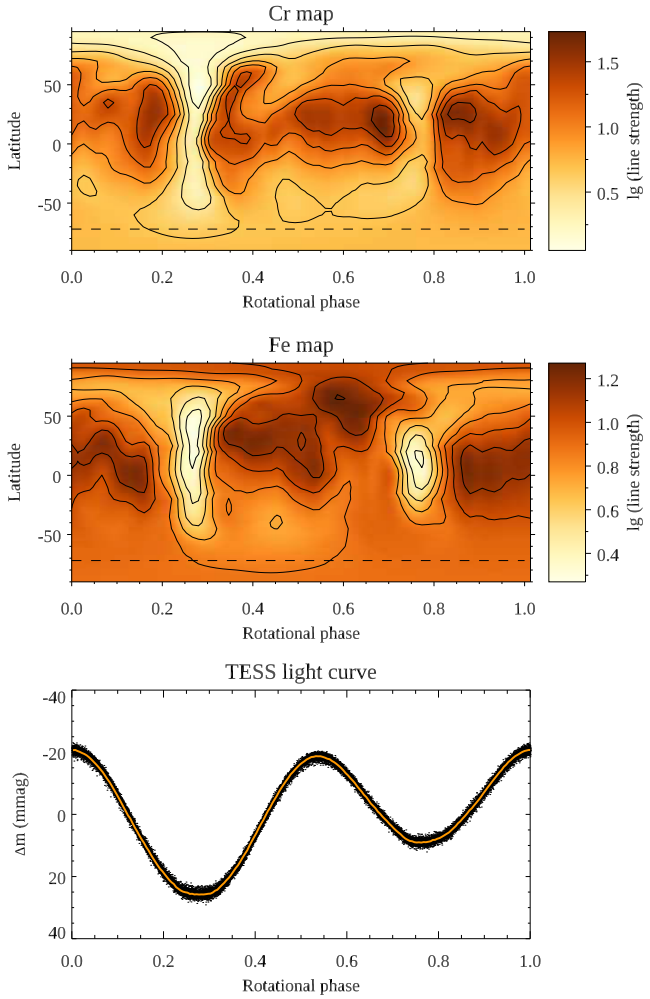

Figure 11. The top two panels show the surface distribution of Cr and Fe, respectively, as a 2D plane, where the *x*-axis gives the rotational phase and the *y*-axis represent the latitude. The dashed line represents the −72° latitude below which the surface of the star is not visible to the line of sight. At the bottom panel, the phased *TESS* light curve of HD 100357 is plotted for comparison.

S/N is increased proportional to the square root of the number of effective absorption lines.

For our study, we computed the LSD profiles for individual elements across the various observed phases for HD 100357. Out of the various sets of LSD profiles calculated for HD 100357, those derived for Cr and Fe exhibit the highest S/N, enabling us to map the surface spots of these elements using DI (Kochukhov 2016). To this end, we employed the DI code `InversLSD` (Kochukhov et al. 2014) to map the distributions of Cr and Fe in terms of the local line strength of the LSD profile. Following the approach of Fréour et al. (2023) and Semenko et al. (2024), the local spectra were computed under the assumption of a Milne–Eddington atmosphere, adopting a Voigt absorption profile. Limb darkening was treated according to the square-root law (Diaz-Cordoves & Gimenez 1992). The RV offset and the projected rotational velocity were refined during the DI analysis by identifying the values that yielded the best fit to the observations.

The results of the DI calculations are presented in Fig. 9 and Fig. 10, which show the fits to the Cr and Fe LSD profiles and the corresponding surface line strength maps, respectively. This analysis yields $\upsilon \sin i$ values of 59.1 and 59.8 $\mathrm{km\,s^{-1}}$ for Cr and Fe, respectively, consistent with other determinations in this study. The maps shown in Fig. 10 indicate that the two elements have qualitatively similar distributions, with Cr exhibiting a higher contrast surface structure. For both elements, the most prominent feature is a ring of relative underabundance encircling the star.

Fig. 11 shows the same Cr and Fe maps as in Fig. 10, but now in a rectangular format with the horizontal axis following the increasing rotational phase. Below the map is the phased *TESS* light curve. It is evident that the areas of relative underabundance for both elements coincide with the light minima. The result agrees with qualitative expectations from theory: a higher abundance increases UV absorption, leading to flux redistribution from UV to optical and NIR (Krtička et al. 2015). Therefore, in the *TESS* bandpass, the star is brighter (fainter) where the element abundance is higher (lower).

6 DISCUSSION AND CONCLUSIONS

We report the detailed study of the Ap star HD 100357, which exhibits an abundance pattern consistent with the typical trends observed in

other hot Ap stars. The star displays slight deficiencies in several light elements. The Fe-peak elements are overabundant by about 1 dex, except for Cr, Mn, and Co, which are overabundant by approximately 2 dex. The neutron capture element Sr is significantly enhanced, with an abundance exceeding the solar value by more than 3 dex. Additionally, the REEs are markedly overabundant, ranging from 3 to 5 dex above their solar values. Also, we found evidence of atomic diffusion through the abundance stratification of Si at different depths. The overabundance of weaker lines of Si indicates a dominance of gravitational settling over radiative levitation.

The Ap stars are distinguished by their excess of Fe-peak elements and REEs. A notable characteristic of hot ($T_{\rm eff} > 10\,000$ K) counterparts in this class is an overabundance of Si. The deficiency of He is also seen in these stars, where the underabundance of He is correlated with the log g of the star (see fig. 4 of Ghazaryan, Alecian & Hakobyan 2018). Similarly, the Fe abundance is correlated to the $T_{\rm eff}$ of the star (see fig. 5 of Ghazaryan et al. 2018). Thus, our target HD 100357 aligns well with all the characteristics of a hot magnetic CP star.

DI analysis revealed a ring of underabundance of Fe and Cr encircling the star. Analogous to the DI results for other Ap stars (Kochukhov, Shultz & Neiner 2019; Kochukhov, Papakonstantinou & Neiner 2022; Kochukhov et al. 2023), these features presumably correspond to the equatorial region of the magnetic axis of a rather weak dipolar-like magnetic field, which is inclined at about 90° to the stellar rotational axis.

Our quantitative examination of individual abundances and qualitative topological abundance distributions indicates that the star is likely to exhibit a detectable magnetic field. Consequently, HD 100357 can be classified as a hot Ap star exhibiting anomalies in Si, Sc, Ti, Cr, Mn, Fe, Co, Sr, and He, or CP2 as per Preston's classification (Preston 1974). The study of these stars aids in comprehending the influence of magnetic fields and rotational forces on stellar atmospheres and chemical composition. Therefore, detailed spectropolarimetric observations are proposed to study the magnetic field topology of HD 100357.

ACKNOWLEDGEMENTS

We are grateful to the Indian and Belgian funding agencies DST (DST/INT/Belg/P-09/2017) and BELSPO (BL/33/IN12) for providing financial support to carry out this work in collaboration. AD acknowledges the financial support received from the DST-INSPIRE Fellowship Programme (DST/INSPIRE Fellowship/2020/IF200245). SJ acknowledges the financial support received from the BRICS grant under the project DST/IC/BRICS/2023/5. SA acknowledges support from the National Natural Science Foundation of China, grant No. W2432009. OK acknowledges support by the Swedish Research Council (grant agreement 2023-03667) and the Swedish National Space Agency. OT acknowledges financial support from the SEISMIC project, the Max Planck–Humboldt Research Unit in collaboration with the Max Planck Institutes for Astrophysics (MPA) and Solar System Research (MPS), and Kyambogo University, as well as from the International Science Programme (ISP) at Uppsala University. This paper includes data collected by the TESS and SIMBAD data bases operated by the NASA Explorer Program and CDS, Strasbourg, France, respectively. The research leading to these results has received funding from the ARC grant for Concerted Research Actions, financed by the Wallonia-Brussels Federation. TRAPPIST is funded by the Belgian Fund for Scientific Research (Fond National de la Recherche Scientifique, FNRS) under the grant PDR T.0120.21. MG and EJ are FNRS-F.R.S. Research Directors. Funding for KB was provided by the European Union (ERC AdG SUBSTELLAR, GA 101054354). We acknowledge the use of the HERCULES spectrograph at the Mt John University Observatory, operated by the University of Canterbury, New Zealand. We acknowledge the use of the High Resolution Spectrograph (HRS) on the Southern African Large Telescope (SALT). This work is based on data obtained from the ESO Science Archive Facility. We acknowledge Dr Donald Wayne Kurtz for his insights into selecting this peculiar candidate from the N-C survey. We express our gratitude to Dr Gautier Mathys for his meticulous assessment and insightful comments regarding this manuscript.

DATA AVAILABILITY

The data underlying this article will be shared upon request to the corresponding author. The *TESS* time-series flux data for the target star are publicly available from the NASA MAST archive (https://mast.stsci.edu/portal/Mashup/Clients/Mast/Portal.html). This work has made use of data from the European Space Agency (ESA) mission *Gaia* (https://www.cosmos.esa.int/gaia), processed by the Gaia Data Processing and Analysis Consortium (DPAC, https://www.cosmos.esa.int/web/gaia/dpac/consortium). Funding for DPAC has been provided by national institutions, in particular those participating in the *Gaia* Multilateral Agreement. This research has also made use of the SIMBAD data base, operated at CDS, Strasbourg, France. This research has used data, tools, or materials developed as part of the EXPLORE project, which has received funding from the European Union's Horizon 2020 research and innovation programme under grant agreement No. 101004214.

REFERENCES

Alecian G., 2018a, MNRAS, 477, 2716
Alecian G., Stift M. J., 2018b, MNRAS, 482, 4519
Ashoka B. N. et al., 2000, Bull. Astron. Soc. India, 28, 251
Aurière M. et al., 2007, A&A, 475, 1053
Bailey J. D., Landstreet J. D., 2013, A&A, 551, A30
Baldry I. K., Kurtz D. W., Bedding T. R., 1998, MNRAS, 300, L39
Baran A. S., Koen C., 2021, Acta Astron., 71, 113
Bernhard K., Hümmerich S., Paunzen E., 2020, MNRAS, 493, 3293
Bessell M. S., 2000, PASP, 112, 961
Bowman D.M. , , Vandenbussche B., Van Reeth T. H. Sana Tkachenko A. Raskin G. Delabie T. Vandoren B. Royer P. Garcia S. Van Reeth T. Collaboration CubeSpec 2022, A&A, 658, A96
Brandt T. D., 2021, ApJS, 254, 42
Cardelli J. A., Clayton G. C., Mathis J. S., 1989, ApJ, 345, 245
Castelli F., 2005, Memorie della Societa Astronomica Italiana Supplementi, 8, 25
Choi J., Dotter A., Conroy C., Cantiello M., Paxton B., Johnson B. D., 2016, ApJ, 823, 102
Crawford S. M. et al., 2010, in Silva D. R., Peck A. B., Soifer B. T.eds, Proc. SPIE Conf. Ser. Vol. 7737, Observatory Operations: Strategies, Processes, and Systems III. SPIE, Bellingham, p. 773725
Diaz-Cordoves J., Gimenez A., 1992, A&A, 259, 227
Dileep A. et al., 2025, MNRAS, 538, 1747
Donati J.-F., Brown S. F., 1997, A&A, 326, 1135
Donati J.-F. et al., 2006, MNRAS, 370, 629
Dotter A., 2016, ApJS, 222, 8
Elkin V. G., Kurtz D. W., Nitschelm C., Unda-Sanzana E., 2010, MNRAS, 401, L44
Fabricius C., Høg E., Makarov V. V., Mason B. D., Wycoff G. L., Urban S. E., 2002, A&A, 384, 180

Fleck R. C., Jr, 1980, ApJ, 240, 218
Fréour L., Neiner C., Landstreet J. D., Folsom C. P., Wade G. A., 2023, MNRAS, 520, 3201
Gaia Collaboration, 2018, A&A, 616, A1
Gaia Collaboration, 2021, A&A, 649, A1
Gaia Collaboration, 2023, A&A 674, A1
Garcia L. J., Timmermans M., Pozuelos F. J., Ducrot E., Gillon M., Delrez L., Wells R. D., Jehin E., 2022, MNRAS, 509, 4817
Ghazaryan S., Alecian G., Hakobyan A. A., 2018, MNRAS, 480, 2953
Giarrusso M., Cecconi M., Cosentino R., Munari M., Ghedina A., Ambrosino F., Boschin W., Leone F., 2022, MNRAS, 514, 3485
Gillon M., Jehin E., Magain P., Chantry V., Hutsemékers D., Manfroid J., Queloz D., Udry S., 2011, in Bouchy F., Díaz R., Moutou C., eds, EPJ Web of Conferences, Vol. 11, Detection and Dynamics of Transiting Exoplanets. EDP Sciences Les Ulis, near Paris, France 06002
Gray R. O., Corbally Christopher J., Princeton University Press Princeton, New Jersey, USA. 2009, Stellar Spectral Classification
Hearnshaw J. B., Barnes S. I., Kershaw G. M., Frost N., Graham G., Ritchie R., Nankivell G. R., 2002, Exp. Astron., 13, 59
Houk N., Cowley A. P., Department of Astronomy, University of Michigan Michigan, USA, 1975, University of Michigan Catalogue of Two-dimensional Spectral Types for the HD Stars. Volume I. Declinations –90_ to –53_.*f*0.
Jehin E. et al., 2011, The Messenger, 145, 2
Joshi S., Joshi Y. C., 2015, JA&A, 36, 33
Joshi S. et al., 2003, MNRAS, 344, 431
Joshi S., Mary D. L., Martinez P., Kurtz D. W., Girish V., Seetha S., Sagar R., Ashoka B. N., 2006, A&A, 455, 303
Joshi S., Mary D. L., Chakradhari N. K., Tiwari S. K., Billaud C., 2009, A&A, 507, 1763
Joshi S., Ryabchikova T., Kochukhov O., Sachkov M., Tiwari S. K., Chakradhari N. K., Piskunov N., 2010, MNRAS, 401, 1299
Joshi S. et al., 2012, MNRAS, 424, 2002
Joshi S. et al., 2016, A&A, 590, A116
Joshi S., Semenko E., Moiseeva A., Sharma K., Joshi Y. C., Sachkov M., Singh H. P., Yerra B. K., 2017, MNRAS, 467, 633
Joshi S. et al., 2022, MNRAS, 510, 5854
Kaufer A., Stahl O., Tubbesing S., Nørregaard P., Avila G., Francois P., Pasquini L., Pizzella A., 1999, The Messenger, 95, 8
Kervella P., Arenou F., Thévenin F., 2022, A&A, 657, A7
Kniazev A. Y., Gvaramadze V. V., Berdnikov L. N., 2016, MNRAS, 459, 3068
Kniazev A. Y., Gvaramadze V. V., Berdnikov L. N., 2017, in Balega Y. Y., Kudryavtsev D. O., Romanyuk I. I., Yakunin I. A.eds, ASP Conf. Ser. Vol. 510, Stars: From Collapse to Collapse. Astron. Soc. Pac., San Francisco, p. 480,
Kochukhov O., 2016, in Rozelot J.-P., Neiner C.eds, Lecture Notes in Physics, Vol. 914, Mapping Stellar Magnetic Fields. Springer-Verlag, Berlin, p. 177
Kochukhov O., 2017, A&A, 597, A58
Kochukhov O., 2018, Astrophysics Source Code Library, record ascl:1805.015
Kochukhov O., Ryabchikova T., 2001, A&A, 374, 615
Kochukhov O., Bagnulo S., Wade G. A., Sangalli L., Piskunov N., Landstreet J. D., Petit P., Sigut T. A. A., 2004, A&A, 414, 613
Kochukhov O., Makaganiuk V., Piskunov N., 2010, A&A, 524, A5
Kochukhov O., Lüftinger T., Neiner C., Alecian E., MiMeS Collaboration, 2014, A&A, 565, A83
Kochukhov O., Shultz M., Neiner C., 2019, A&A, 621, A47
Kochukhov O., Papakonstantinou N., Neiner C., 2022, MNRAS, 510, 5821
Kochukhov O., Gürsoytrak Mutlay H., Amarsi A. M., Petit P., Mutlay I., Gürol B., 2023, MNRAS, 521, 3480
Krtička J., Mikulášek Z., Lüftinger T., Jagelka M., 2015, A&A, 576, A82
Kunzli M., North P., Kurucz R. L., Nicolet B., 1997, A&AS, 122, 51
Kurtz D. W., 2000, ARA&A, 38, 531
Kurtz D.W. , 60, inAnnual Review of Astronomy and Astrophysics Annual Review of Astronomy and Astrophysics California, USA Asteroseismology Across the Hertzsprung-Russell Diagram 2022 31–71,
Kurucz R. L., 2005, Memorie della Societa Astronomica Italiana Supplementi, 8, 14
Lallement R., Vergely J. L., Babusiaux C., Cox N. L. J., 2022, A&A, 661, A147
Landstreet J. D., Bagnulo S., Andretta V., Fossati L., Mason E., Silaj J., Wade G. A., 2007, A&A, 470, 685
Lenz P., Breger M., 2005, CoAst, 146, 53
Lenz P., Breger M., 2014, Astrophysics Source Code Library, record ascl:1407.009
Lightkurve Collaboration 2018, Astrophysics Source Code Library, record ascl:1812.013
Lodders K., 2021, Space Sci. Rev., 217, 44
Martinez P. et al., 2001, A&A, 371, 1048
Mason B. D., Wycoff G. L., Hartkopf W. I., Douglass G. G., Worley C. E., 2001, AJ, 122, 3466
Mathys G., 2017, A&A, 601, A14
Mathys G., Holdsworth D. L., Giarrusso M., Kurtz D. W., Catanzaro G., Leone F., 2024, A&A, 691, A186
Mermilliod J. C., Mermilliod M., Hauck B., 1997, A&AS, 124, 349
Michaud G., 1970, ApJ, 160, 641
Miglio A., Montalbán J., Dupret M. A., 2007, Commun. Asteroseismol., 151, 48
Mikulášek Z., Semenko E., Paunzen E., Hümmerich S., North P. L., Bernhard K., Krtička J., Janík J., 2022, A&A, 668, A159
Mkrtichian D. E., Hatzes A. P., Kanaan A., 2003, MNRAS, 345, 781
Munari U., Zwitter T., 1997, A&A, 318, 269
Napiwotzki R., Schoenberner D., Wenske V., 1993, A&A, 268, 653
Netopil M., Paunzen E., Maitzen H. M., North P., Hubrig S., 2008, A&A, 491, 545
Norris J., 1971, ApJS, 23, 213
Pakhomov Y. V., Ryabchikova T. A., Piskunov N. E., 2019, Astron. Rep., 63, 1010
Paxton B., Bildsten L., Dotter A., Herwig F., Lesaffre P., Timmes F., 2011, ApJS, 192, 3
Paxton B. et al., 2013, ApJS, 208, 4
Paxton B. et al., 2015, ApJS, 220, 15
Paxton B. et al., 2018, ApJS, 234, 34
Piskunov N. E., Kupka F., Ryabchikova T. A., Weiss W. W., Jeffery C. S., 1995, A&AS, 112, 525
Preston G. W., 1974, ARA&A, 12, 257
Richard O., Michaud G., Richer J., 2001, ApJ, 558, 377
Ricker G. R. et al., 2015, J. Astron. Telesc. Instrum. Syst., 1, 014003
Romanyuk I. I., Semenko E. A., Kudryavtsev D. O., Moiseeva A. V., Yakunin I. A., 2013, Astrophys. Bull., 68, 300
Ryabchikova T., Pero Moscow, Russia 2014, in Mathys G., Griffin E. R., Kochukhov O., Monier R., Wahlgren G. M.eds, Putting A Stars into Context: Evolution, Environment, and Related Stars. p. 220
Ryabchikova T., Nesvacil N., Weiss W. W., Kochukhov O., Stütz C., 2004, A&A, 423, 705
Ryabchikova T., Ryabtsev A., Kochukhov O., Bagnulo S., 2006, A&A, 456, 329
Ryabchikova T., Piskunov N., Kurucz R. L., Stempels H. C., Heiter U., Pakhomov Y., Barklem P. S., 2015, Phys. Scr, 90, 054005
Saio H., 2005, MNRAS, 360, 1022
Semenko E. et al., 2024, MNRAS, 535, 2812
Shultz M., Wade G. A., Rivinius T., Sikora J., Oksala M. E., Bohlender D., Neiner C., 2019, MNRAS, 490, 274
Sikora J., Wade G. A., Power J., Neiner C., 2019, MNRAS, 483, 3127
Skuljan J., 2004, in Kurtz D. W., Pollard K. R.eds, ASP Conf. Ser. Vol. 310, IAU Colloq. 193: Variable Stars in the Local Group. Astron. Soc. Pac., San Francisco, p. 575
Smith J. C. et al., 2012, PASP, 124, 1000
Stibbs D. W. N., 1950, MNRAS, 110, 395
Sullivan P. W. et al., 2015, ApJ, 809, 77

Torres G., 2010, AJ, 140, 1158
Tsymbal V., Ryabchikova T., Sitnova T., 2019, in Kudryavtsev D. O., Romanyuk I. I., Yakunin I. A.eds, ASP Conf. Ser. Vol. 518, Physics of Magnetic Stars. Astron. Soc. Pac., San Francisco, p. 247
Tyas L. M. G., 2012, PhD thesis, Durham University
Vauclair S., Vauclair G., 1975, A&A, 45, 233
Vergely J. L., Lallement R., Cox N. L. J., 2022, A&A, 664, A174
Zboril M., North P., 1997, A&A, 318, 950

APPENDIX A: INDIVIDUAL LINE ABUNDANCES

Table A1. The LTE abundances of HD 100357 derived from individual spectral lines of chemical species. The column [X/H] represents the abundance $\log(A)_X$ relative to the solar abundances.

Atomic number	Element	Wavelength (Å)	$\log(A)_X$	[X/H]	Solar abundance
2	He II	5875	−3.1	−2	−1.1
2	He II	4471	−3.1	−2	−1.1
6	C II	4267.259	−4.7	−1.28	−3.42
8	O I	7771–7775	−4.27	−1.03	−3.24
12	Mg II	4481	−5.2	−0.7	−4.5
12	Mg II	7877.054	−5	−0.5	−4.5
12	Mg II	7896.366	−4.9	−0.4	−4.5
13	Al II	4663.046	−5.94	−0.35	−5.59
13	Al II	5593.2998	−6	−0.41	−5.59
13	Al II	7042.083	−6	−0.41	−5.59
14	Si II	4130.872	−3.83	0.65	−4.48
14	Si II	4130.894	−3.83	0.65	−4.48
14	Si II	4621.418	−3.45	1.03	−4.48
14	Si II	4621.7222	−3.45	1.03	−4.48
14	Si II	5041.0239	−3.74	0.74	−4.48
14	Si II	5055.9839	−4.13	0.35	−4.48
14	Si II	5056.3169	−4.13	0.35	−4.48
14	Si II	5688.817	−3.4	1.08	−4.48
14	Si II	5800.454	−3.31	1.17	−4.48
14	Si II	5806.731	−3.66	0.82	−4.48
14	Si II	5867.48	−3.4	1.08	−4.48
14	Si II	5868.4438	−3.4	1.08	−4.48
14	Si II	5957.5591	−4	0.48	−4.48
14	Si II	6371.3711	−4.2	0.28	−4.48
14	Si II	6660.532	−3.43	1.05	−4.48
14	Si II	6671.841	−3.6	0.88	−4.48
14	Si II	6699.431	−3.3	1.18	−4.48
14	Si II	7848.816	−4	0.48	−4.48
14	Si II	7849.722	−4	0.48	−4.48
14	Si III	4567.84	−3.5	0.98	−4.48
15	P II	4602	−5.6	0.98	−6.58
15	P II	6165.598	−5.5	1.08	−6.58
16	S II	5453.855	−4.3	0.58	−4.88
16	S II	5606.151	−4.2	0.68	−4.88
21	Sc II	4374.457	−7.15	1.7	−8.85
21	Sc II	4400.3892	−7.29	1.56	−8.85
21	Sc II	5526.79	−7.36	1.49	−8.85
22	Ti II	4163.644	−6.4	0.63	−7.03
22	Ti II	4443.801	−6.2	0.83	−7.03
22	Ti II	4468.493	−6.4	0.63	−7.03
22	Ti II	4571.972	−6.12	0.91	−7.03
24	Cr II	4145.7808	−4	2.38	−6.38
24	Cr II	4242.366	−4	2.38	−6.38
24	Cr II	4256.1079	−4.23	2.15	−6.38
24	Cr II	4275.5669	−4.1	2.28	−6.38
24	Cr II	4511.7749	−4.01	2.37	−6.38

Table A1 – *continued*

Atomic number	Element	Wavelength (Å)	$\log(A)_X$	[X/H]	Solar abundance
24	Cr II	4539.595	−4.15	2.23	−6.38
24	Cr II	4592.052	−4.3	2.08	−6.38
24	Cr II	4616.6289	−4.02	2.36	−6.38
24	Cr II	4812.3369	−4.25	2.13	−6.38
24	Cr II	4824.127	−4.04	2.34	−6.38
24	Cr II	5420.925	−4.06	2.32	−6.38
25	Mn I	4030.7529	−4.45	2.1	−6.55
25	Mn II	4251.7168	−4.57	1.98	−6.55
25	Mn II	4252.9629	−4.57	1.98	−6.55
25	Mn II	4292.2368	−4.43	2.12	−6.55
25	Mn II	4478.6372	−4.43	2.12	−6.55
25	Mn II	4518.956	−4.53	2.02	−6.55
25	Mn II	4727.84	−4.6	1.95	−6.55
25	Mn II	4738.29	−4.5	2.05	−6.55
25	Mn II	4749.112	−4.51	2.04	−6.55
25	Mn II	4755.727	−4.31	2.24	−6.55
25	Mn II	4764.728	−4.45	2.1	−6.55
25	Mn II	4784.625	−4.5	2.05	−6.55
26	Fe II	4461.706	−3.25	1.23	−4.48
26	Fe II	4520.218	−3.52	0.96	−4.48
26	Fe II	4522.628	−3.27	1.21	−4.48
26	Fe II	4596.01	−3.34	1.14	−4.48
26	Fe II	4638.041	−3.17	1.31	−4.48
26	Fe II	4977.03	−3.11	1.37	−4.48
26	Fe II	5325.552	−3.26	1.22	−4.48
26	Fe II	5387.063	−3.46	1.02	−4.48
26	Fe II	5487.618	−3.46	1.02	−4.48
26	Fe II	5830.344	−3.39	1.09	−4.48
26	Fe II	5838.99	−3.3	1.18	−4.48
26	Fe II	5871.77	−3.26	1.22	−4.48
26	Fe II	6060.967	−3.3	1.18	−4.48
26	Fe II	7506.543	−3.46	1.02	−4.48
27	Co II	4569.25	−5	2.04	−7.04
27	Co II	4660.656	−5	2.04	−7.04
28	Ni I	4980.166	−5.8	−0.080	−5.72
28	Ni I	5080.527	−5.79	−0.070	−5.72
28	Ni I	5081.1069	−5.81	−0.090	−5.72
38	Sr II	4215.519	−5.41	3.67	−9.08
60	Nd III	4927.4877	−7.34	3.21	−10.55
60	Nd III	5294.1133	−7.2	3.35	−10.55
64	Gd II	4514.504	−5.74	5.15	−10.89
64	Gd II	4193.145	−5.5	5.39	−10.89
66	Dy II	4573.855	−6.92	3.95	−10.87
66	Dy II	4073.12	−6.95	3.92	−10.87

APPENDIX B: CONTAMINATION

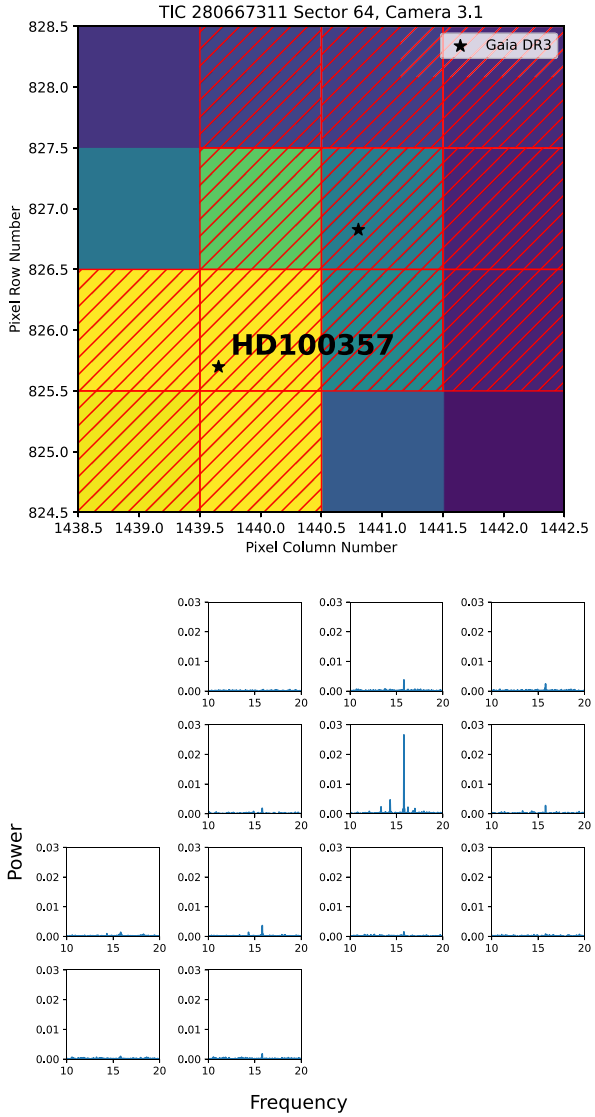

Figure B1. Top panel: the *TESS* pixels (4 × 4, Sector 10) in the field of HD 100357 marked with a star symbol and labelled. To the top right, a nearby star is seen contaminating HD 100357. The hatched pixels show the masks used to plot the periodograms in the bottom panel. Bottom panel: the corresponding periodograms of the selected masks. We can see the increased amplitude of the contaminating frequency at the pixel with the contaminating star and the amplitude drops towards the target star.

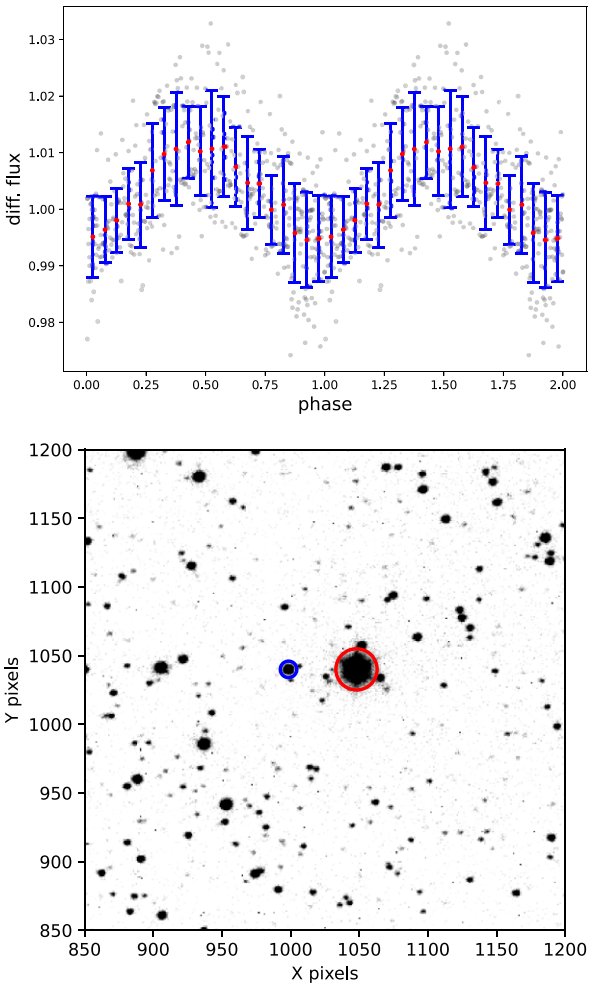

Figure B2. Top panel: the ground-based phased light curve of the contaminating star observed with TRAPPIST-South folded with the contaminating period. The red dots show the binned light curve, while the blue error bars are standard deviations in each bin. The grey dots in the background are the original phased light curve. Bottom panel: a cut-out of *R*-band CCD image in the field of HD 100357 taken with TRAPPIST-South. The larger red circle to the right is HD 100357 and the smaller blue circle to the left is *Gaia* DR3 5236626819707864192, which contaminates HD 100357 in *TESS* pixels.

This paper has been typeset from a TEX/LATEX file prepared by the author.